

Article

An Efficient Photocatalyst for Fast Reduction of Cr(VI) by Ultra-Trace Silver Enhanced Titania in Aqueous Solution

Shengyan Pu ^{1,2,*} , Yaqi Hou ¹, Hongyu Chen ¹, Daili Deng ¹, Zeng Yang ¹, Shengyang Xue ¹, Rongxin Zhu ¹, Zenghui Diao ^{2,3} and Wei Chu ²

¹ State Key Laboratory of Geohazard Prevention and Geoenvironment Protection, Chengdu University of Technology, Chengdu 610059, China; houyaqilove@gmail.com (Y.H.); chenhongyu98@163.com (H.C.); dengdaili.1022@gmail.com (D.D.); yangzeng199529@gmail.com (Z.Y.); shengyangxue@gmail.com (S.X.); rongxinzhu@outlook.com (R.Z.)

² Department of Civil and Environment Engineering, The Hong Kong Polytechnic University, Hong Kong, China; zenghui86@scsio.ac.cn (Z.D.); wei.chu@polyu.edu.hk (W.C.)

³ School of Environmental Science and Engineering, Zhongkai University of Agriculture and Engineering, Guangzhou 510225, China

* Corresponding: pushengyan@gmail.com or pushengyan13@cdut.cn; Tel./Fax: +86-(0)-28-8407-3253

Received: 10 May 2018; Accepted: 14 June 2018; Published: 19 June 2018



Abstract: For the purpose of establishing a simple route to prepare a metal-semiconductor hybrid catalyst efficiently and reduce its cost through precise doping noble metals. In this study, ultra-trace silver doped TiO₂ photocatalysts were fabricated via a “green” ultrasonic impregnation-assisted photoreduction strategy in an ethanol system, and its photocatalytic performance was systematically investigated by utilizing Cr(VI) as the model contaminant. A schottky energy barrier was constructed in Ag@TiO₂, which served as a recombination center and possessed superior photocatalytic activity for Cr(VI) reduction. The obtained catalysts exhibited a significant e^-/h^+ separation efficiency which directly led to an obvious photocatalytic property enhancement. Then, the resultant Ag@TiO₂ (0.06 wt %, 30 min irradiation) showed about 2.5 times the activity as that of commercial P25 NPs for Cr(VI) degradation. Moreover, after five cycles, it still maintained considerably high catalytic ability (62%). This work provides a deep insight into preparation techniques of metal-semiconductor photocatalyst and broadens their application prospect.

Keywords: Ag@TiO₂; Cr(VI) reduction; in-situ photoreduction; ultrasonic impregnation; ultra-trace silver

1. Introduction

Nowadays, heavy metals pollution in aquatic environments poses serious risks to public health and ecological systems since the rapid development of industrialization [1]. As a non-degradable and toxic metal ion, Cr(VI) has been commonly identified in aquatic circumstances, due to its carcinogenic, mutagenic and teratogenic effects on living creatures [2]. The Ministry of Ecology and Environment of the People’s Republic of China and World Health Organization (WHO) have regulated the maximum concentration authorized in drinking water as being below 0.05 mg/L (Sanitary Standard for Drinking Water Quality (2001)) [3,4]. However, the inevitable drawbacks of high cost or secondary contamination still exist among conventional methods to remove heavy metals from aqueous solutions, such as chemical reduction [5,6], membrane separation [7], electrolytic [8], ferrite method [9,10], precipitation [11], adsorption [12,13], ion exchange [14] and biological method [15]. Hence, it is important to explore a cost-efficient method for Cr(VI) removal.

Heterogeneous photocatalysis is achieved by the excitation of electrons from semiconductors' valence band (VB) to the conduction band (CB) upon light irradiation, wherein the excited electrons and holes can be directly applied in redox processes. Owing to the highly reductive property of photo-generated electrons, photocatalysis [16] can be served as a desirable reductive. Compared to the conventional methods, it has relatively broader application prospects due to its recyclable and non-secondary pollution advantages [17]. For example, reduced graphene oxide and ZnO hybrids (RGO/ZnO) was utilized in different particle sizes for photocatalytic reduction of Cr(VI) [18]. In parallel, the photocatalytic Pb(II) reduction over WO_3/TiO_2 nanomaterials, the reduction capacity was increased from 52.2% to 74.7% via WO_3 doping [19]. Moreover, The photocatalytic removal of heavy metal ions by TiO_2 nanotubes could be further enhanced through Cu^{2+} loadings [20].

Furthermore, to improve the semiconductors' catalytic performance [21], the noble metal deposition [22] recently has been proven to be a predominant way to heighten the activity of photocatalysis by creating the Schottky barrier at the semiconductor metal interface, which helps in separating the photo-excited electrons in the CB onto the metal nanoparticles (NPs) [23]. During the past decade, various noble metals such as Pt, Au, and Ag have been frequently immobilized on TiO_2 [24,25] or other semiconductors to enhance their photocatalytic performance. However, among a wide variety of metal-semiconductor hetero-structures [26], Ag@TiO_2 [27] photocatalysts aroused tremendous attention as they showed the most efficient plasmon resonance which was favorable for catalytic enhancement [28]. Therefore, various methods to obtain Ag@TiO_2 composites have been developed, such as hydrothermal [29], sol-gel [30], magnetron co-sputtering [31], photodeposition [32], sedimentation and impregnation [33]. These methods are usually either complex or require rather extreme conditions to operate. To obtain an efficient Ag@TiO_2 photocatalyst, the silver dosage is still relatively high (>1 wt %), which greatly elevates its cost and limits its actual application. For instance, Chen and Zhang [30] synthesized an Ag@TiO_2 compound through a novel one-pot sol-gel strategy with 3.9 wt % silver addition and systematically studied its potent antibacterial activities. Liu et al. [34] demonstrated the deposition of Ag nanoparticles on TiO_2 nanofibers with 4.65 wt % silver dosage by a facile polyol synthesis, and the result showed superior natural antibacterial activity and high-performance photocatalytic disinfection under solar irradiation. Considering the conventional complex procedures and high silver consumption in Ag@TiO_2 preparation, how to simplify the fabrication steps and control the silver doping amount would be the crucial steps to control the cost and broaden the practical application of Ag@TiO_2 . Particularly, how to obtain an efficient catalyst under an ultra-trace noble metal deposition.

In this work, a facile photoreduction strategy was utilized to in situ synthesize Ag@TiO_2 photocatalysts with ultra and exhibited superior photocatalytic activity on reducing highly toxic Cr(VI) to low-toxic Cr(III). The photoreduction properties of Ag@TiO_2 were evaluated in different influencing parameters, such as the amount of Ag, the initial pH of solution, the amount of catalyst dosage, the light intensity and the coexisting ions. The results shown that the synthesized Ag@TiO_2 bears good Cr(VI) reduction performance, which provides a deep insight for the application of photocatalysis in wastewater treatment.

2. Results and Discussion

2.1. Preparation and Characterizations of Ultra-Trace Silver Enhanced Titania Photocatalyst

The ultra-trace silver doped TiO_2 photocatalysts were prepared via a "green" ultrasonic impregnation assisted photoreduction strategy, as shown in Figure 1. Firstly, the color of ethanol and TiO_2 mixture maintained no change under dark conditions after AgNO_3 addition. During the illuminated period, the mixture's color gradually turned from initial ecru to light blue (the color of products gradually deepened with the Ag dosage increasing, such as yellow-brown, purple-brown, etc., which mainly due to the photogenerated electrons (e^-) assisted Ag^+ reduction process (Figure 1a).

Then, the obtained catalysts were used for Cr(VI) reduction (Figure 1b). Cr(VI) was first adsorbed on the surface of Ag@TiO₂, and then Cr(VI) was reduced to Cr(III) gradually by the CB formed e^- .

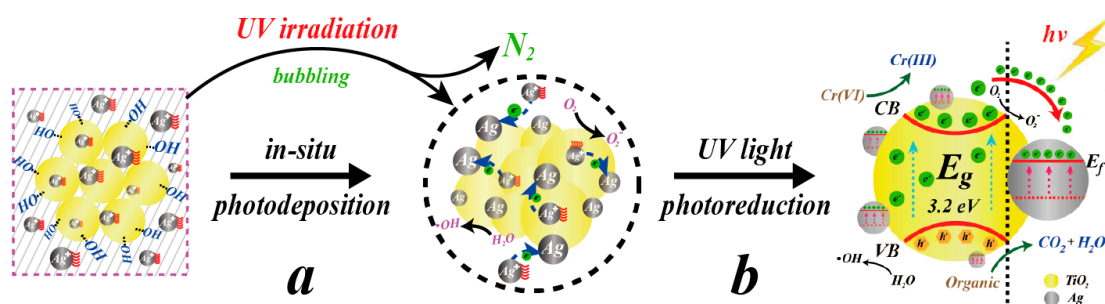


Figure 1. Schematic illustration of (a) synthesis of ultra-trace silver doped TiO₂ composites via ultrasonic impregnation assisted deposition through an in situ UV-assisted photoreduction strategy; (b) photoreduction of highly toxic Cr(VI) to nontoxic Cr(III) by resultant Ag@TiO₂ photocatalysts under UV irradiation.

Figure 2a shows the typical morphology and surface composition of the resultant Ag@TiO₂ compound. The transmission electron microscope (TEM) image clearly shows the sphere-like synthesized material with an average diameter of ca. 24.5 ± 2 nm. High resolution transmission electron microscope (HRTEM, Figure 2b) observation revealed that TiO₂ nanoparticles crystallized well with a lattice fringes spacing of 0.35 nm, which well matches the d -spacing of (111) plane of TiO₂ ($d = 0.35$ nm). Furthermore, the d -spacing of 0.235 nm could be found either which fits the (001) plane d spacing of TiO₂ ($d = 0.235$ nm) and no obvious Ag nanoparticles could be found since the rather trace silver addition of 0.06 wt %. However, as shown in Figure S1 and Table 1, silver nanoparticles exist on the surface of TiO₂. According to the BET surface area analysis (Tables S1 and S2), the Ag doping ratio and h^+ scavenger (ethanol) concentration do not influence the specific surface area of Ag@TiO₂ obviously.

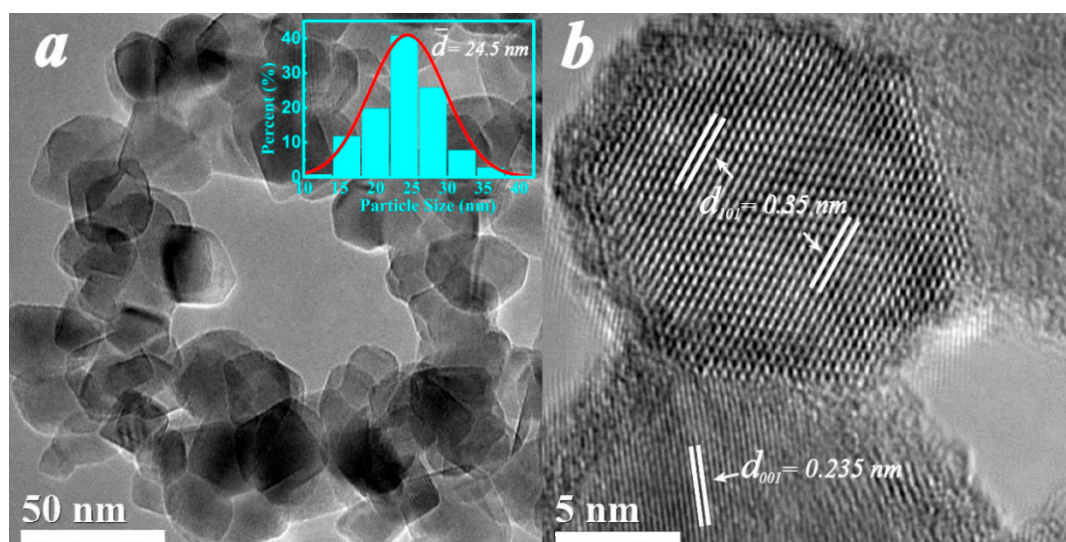


Figure 2. (a) TEM image of Ag@TiO₂ (0.06 wt %, 30 min radiation) and NPs size distribution graphic (obtained by counting 114 Ag@TiO₂ particles); (b) HRTEM images of the prepared Ag@TiO₂ composites, $d_{001} = 0.235$ nm, $d_{101} = 0.35$ nm.

Table 1. ICP-AES data of Ag@TiO₂.

Mass/g	Volume/mL	Dilution Factor	Element	Readings mg/L	Conversion mg/kg	Ag/TiO ₂ wt %
0.0164	50	1 50	Ag	0.1778	542.03	0.0648
			Ti	3.2883	501260.67	

Considering the mild experimental conditions, the obtained nanocomposites exhibited similar X-ray diffraction (XRD) patterns to the pure TiO₂, as shown in Figure 3 and Figure S2. Specifically, the peaks of Ag@TiO₂ at 2θ values of 25.1°, 37.6°, 47.9°, 53.7°, 55.1°, 62.6°, 68.8°, 70.1°, and 75.0° might belong to (101), (004), (200), (105), (211), (204), (116), (220), and (215) crystal planes of anatase phase (JCPDS Card No. 21-1272), respectively. Moreover, the peaks at 27.4° and 36.0° were ascribed to the (110) and (101) planes of rutile phase (JCPDS Card No. 21-1276). In comparison to bare TiO₂, the peaks at 2θ value of 38.1°, 44.23°, 64.4°, and 77.4° could be found, which belong to the (111), (200), (220), and (311) planes of Ag (JCPDS card number: 04-0783), respectively. However, since the Ag addition was rather low and overlapping by the TiO₂ characteristic peak at 38.1°, these peaks were relatively weak in the XRD pattern. Finally, according to the XRD and TEM analyses above, the results revealed that Ag nanoparticles were formed and successfully loaded on the TiO₂ surface.

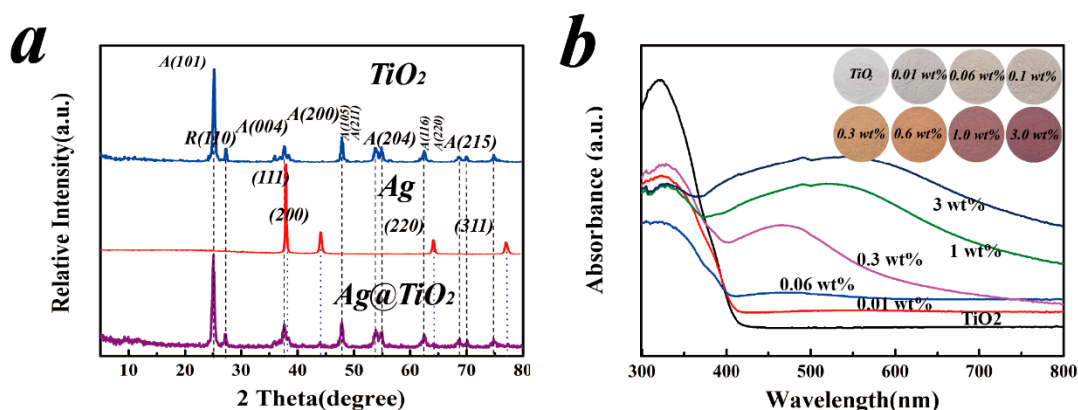


Figure 3. (a) XRD patterns of the Ag@TiO₂ photocatalysts, in which A is anatase phase and R is rutile phase (no obvious Ag characteristic peak was found due to the ultra-trace loaded amount); (b) UV-vis diffuse spectra of Ag@TiO₂ in different doping ratio (dried sample images with different Ag loadings, insert).

It was noteworthy that the obvious improvement of visible light absorption in the range of 400–700 nm could be noticed under the addition of Ag, which fits the gradual color change from ecru to purple (Figure 3b, insert). A significant optical adsorption enhancement could be observed in different Ag contents of 0.3 wt %, 1.0 wt % and 3.0 wt %, whose absorption peaks appeared as a red shift moved from 480 nm to 580 nm. However, there were almost no differences between Ag@TiO₂ doping ratios of 0.01 wt % and 0.06 wt %, which were similar to bare TiO₂. The observed peaks should be attributed to the surface plasmon resonance (SPR) effect of spatially confined electrons in Ag nanoparticles and this red-shift might be related to the interaction between Ag and TiO₂. Moreover, the adsorption peak range might be continuously broadened as the Ag dosage increases.

2.2. Catalytic Activity for Cr(VI) Photoreduction

The catalytic properties of Ag@TiO₂ photocatalysts were evaluated by Cr(VI) imitated heavy metal wastewater. As shown in Figure 4a, Cr(VI) was firstly adsorbed onto the surface of Ag@TiO₂ and adsorption equilibrium could be reached within 30 min under dark conditions. The aquatic Cr(VI) could be fully reduced to Cr(III) within 60 min under UV irradiation. The results illustrated that the Cr(VI) photocatalytic reduction efficiency got improved through Ag loading, which might be due

to the following reasons. The photoresponse range could be enhanced, as presented in Figure 3b. Then, the Schottky junction would be formed at the interface with Ag deposition. Under light irradiation, photo-generated electrons (e^-) tend to migrate and accumulate on Ag nanoparticles which served as effective electron acceptors, and the extra acceptors subsequently promoted the e^-/h^+ separation efficiency and ultimately enhanced the photocatalytic reduction of Cr(VI). It is noteworthy that the amount of metal deposition has a great influence on the photocatalytic ability of the obtained photocatalysts. However, the photocatalytic efficiency gradually decreases once the Ag loading exceeds 0.06 wt %, which is mainly due to the shielding effect by the excessive Ag coverage. In addition, when the Ag doping ratio gets higher (>0.06 wt %), the extra Ag sites tend to act as the e^-/h^+ recombination centers which may lead to the recombination enhancement and result in photon quantum efficiency drop. The effect of different concentration of Ethanol on Cr(VI) reduction is shown in Figure S3. Figure 4b shows that the maximum UV-visible absorption of Cr(VI) solution was at 545 nm, which was close to the standard value of 540 nm. It can be obviously noticed that the Cr(VI) absorbance decreased rapidly in the first 20 min, but slowly later on.

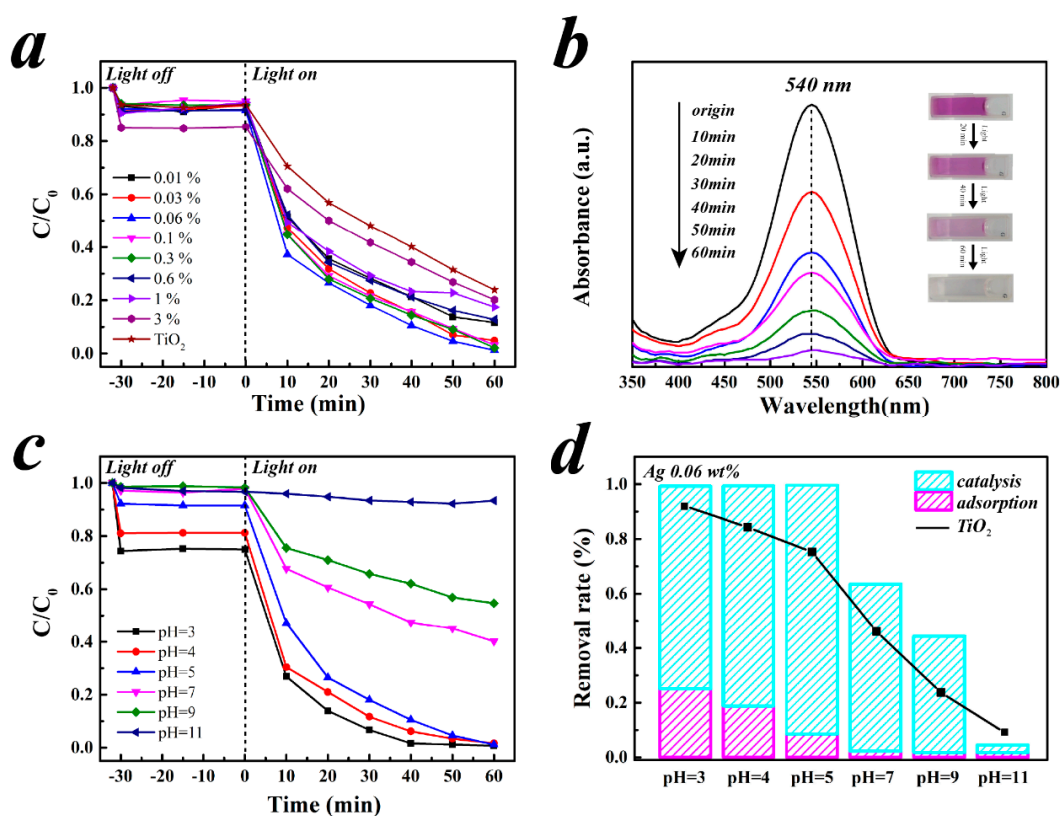


Figure 4. (a) Photocatalytic reduction efficiency by pure TiO_2 and Ag@ TiO_2 composites with various Ag loading ratio (effect of different loading on adsorption balance before irradiation, insert); (b) UV-vis full wave band scanning of Cr(VI) under different irradiation times (the color change of Cr(VI) simples with different reduction time, insert); (c) Effect of different initial pH on Cr(VI) reduction rate; (d) The contribution of adsorption and photoreduction in Cr(VI) removal with different initial pH value using bare TiO_2 and Ag@ TiO_2 . (Both (b,c,d) using the simple with 0.06 wt % Ag addition. The experimental conditions were $[Cat] = 1 \text{ g/L}$, $[Cr(VI)]_0 = 10 \text{ mg/L}$, 300 W and 60 min irradiation.

The impact of the initial pH on the Cr(VI) reduction was investigated, and its degradation efficiency was gradually reduced with pH increasing from 3.0 to 11.0 (Figure 4c,d). Therefore, the initial pH plays a significant role in the whole Cr(VI) photocatalytic reduction processes, which not only affects the surface adsorption but also the chromium's redox potential [35]. On the other hand, as the

main catalytic reaction occurred on the interface, the adsorption ability to substrates would be a crucial role in the migration and captures of photogenerated carriers, which would directly affect the surface reactivity in the following photocatalytic reaction processes [36]. First of all, the Cr(VI) adsorption procedure was the prerequisite step for photocatalytic reduction, and the influence of initial pH on adsorption as well as resultant removal rate are shown in Figure 4d. Cr(VI) interface adsorption rapidly increases with pH decreasing. The maximum adsorption rate of 25% (pH = 3) was five times that of the lowest one 1% (pH = 11). This phenomenon was mainly due to the electrostatic attraction that the negatively charged $\text{Cr}_2\text{O}_7^{2-}$ would spontaneously attach to positively charged subjects. According to the ζ potential testing in (Figure S4), the pH_{pzc} (pH of zero-point charge) value of Ag@TiO_2 was 5–6. So, when initial pH <5, the surface would be positively charged which was in favor of the $\text{Cr}_2\text{O}_7^{2-}$ adsorption. On the contrary, its surface would become negatively charged when pH >5, which will result in a decrease in the adsorption capacity of Cr(VI). Therefore, it could be concluded that the adsorption capacity for Cr(VI) plays an important role in the photoreduction processes.

On the other hand, the metal pair's redox potential was either a significant factor that determines the photocatalytic ability of the resultant composites. As shown in Figure 4c, the Cr(VI) photoreduction rate gradually drops with pH increasing. Specifically, the equilibrium could be reached within 40 min under the condition of pH = 3, but no obvious reduction could be found at pH = 11, which indicated that the oxidation ability of Cr(VI) was strongly affected by the H^+ concentration. Moreover, as the initial pH got higher, the redox potential of Cr(VI) decreased which leads to the drop of its oxidation ability (See Supplementary Materials, Equations (S1)–(S3)). It could be concluded that the photoreduction of Cr(VI) should be easier under acidic conditions and relatively difficult under neutral or alkaline conditions could be drawn. And, it also indicated that the negative effect of the proton deficiency could be inhibited via providing enough protons to the reaction system. Moreover, it is noteworthy that Ag@TiO_2 exhibits a higher photocatalytic activity than pure TiO_2 at the same pH (Figure 4d, line), which may be due to the available free electrons on the Ag@TiO_2 surface or the active sites that can donate electrons to Cr(VI) being more than pure TiO_2 . Therefore, the initial pH impact on Cr(VI) reduction came from the integrative actions of various changes in the physicochemical properties of all the substances involved. The high efficiency of the obtained ultra-trace Ag doped TiO_2 photocatalyst under acidic, neutral and alkaline conditions suggests its promising potential for wastewaters purification and treatment.

The effect of the catalyst dosage on Cr(VI) reduction is shown in Figure 5a, the Cr(VI) reduction efficiency exhibited a positive dependence on the Ag@TiO_2 dosage. There was not any reduction that could be detected in the absence of catalyst addition and the Cr(VI) removal efficiency gradually increased with dosage increasing. When the dosage was increased to 2 g/L, Cr(VI) could be fully reduced to Cr(III) within 30 min, and the removal rate could still reach above 75% at a lower dosage (0.5 g/L). It was mainly due to that the increasing dosage providing more reaction sites for Cr(VI) adsorption and photoreduction, as well as to producing more photogenerated electrons.

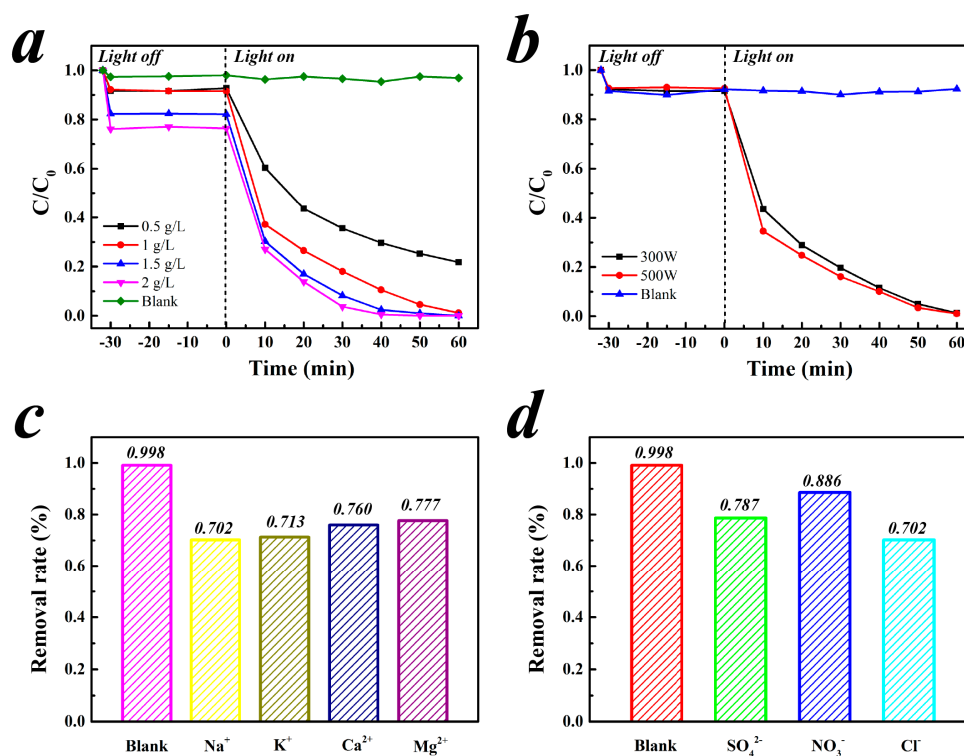


Figure 5. (a) Photocatalytic reduction of Cr(VI) by Ag@TiO₂ composites of various dosages (the blank sample catalytic system showed that no obvious Cr(VI) degradation could be observed under UV irradiation); (b) Effect of illumination on Cr(VI) reduction; (c) Removal rate of co-existing cations on Cr(VI) reduction efficiency (metal salts: NaCl, KCl, MgCl₂, CaCl₂); (d) Removal rate of co-existing anions on Cr(VI) reduction efficiency (metal salts: NaCl, Na₂SO₄, NaNO₃); Both (a–d) using the Ag@TiO₂ with 0.06 wt %. The experimental conditions were [Cr(VI)]₀ = 10 mg/L, initial pH = 5.

Figure 5b shows the Cr(VI) photocatalytic reduction under the UV-light intensity that varied from 0 W (blank) to 500 W. The removal rate for adsorption was maintained obviously at less than 10% until the equilibrium and the photoreduction was significantly improved under UV-light compared to the blank one. However, it should be noted that there are little differences between the 300 W and 500 W mercury lamps although the intense illumination might facilitate electron production. The Cr(VI) removal efficiency could reach about 95% within 50 min under the illumination intensities 300 W or 500 W. Therefore, it would be more advisable to utilize the 300 W lamp for considering the energy consuming.

Since industrial wastewater contains a variety of conventional materials which are usually comprised of routine anions and cations, these co-existing substances tend to reduce the catalytic performance of Ag@TiO₂ composites. To explore the potential synergistic effect between co-existing ions and Ag@TiO₂ composites, a series of co-existing ions, such as Cl⁻, SO₄²⁻, NO₃⁻ and Na⁺, K⁺, Mg²⁺, Ca²⁺ ions were utilized in the control group. As the amount of co-existing ions in practical industrial wastewater usually reaches thousands of ppm, in order to imitate the actual situation, its concentrations are all set at 0.1 mol/L, which in turn may affect the rate of photocatalytic reduction.

As illustrated in Figure 5c, all co-existing ions have a significant impact on the Cr(VI) reduction process. Two sequences on the impact of co-existing ions were drawn through experiments, like Cl⁻ > SO₄²⁻ > NO₃⁻ and Na⁺ > K⁺ > Ca²⁺ > Mg²⁺. The main reason for the inhibiting effect by co-existing anions was the competition between anionic and dichromate adsorption and active sites on the surface. To be more specific, NO₃⁻ have very few effects whereas SO₄²⁻ or Cl⁻ were more rapidly adsorbed by the catalyst than Cr(VI), which is similar to a previous report [37]. Obviously, the Na⁺ introduced together has a certain influence on the removal rate of the experiment (Figure 5d). As for

cations, the impacts on photoreduction can be neglected since Na^+ , K^+ , Mg^{2+} and Ca^{2+} ions are already in their highest oxidation states, so they can neither capture radicals or photo-generated holes [38]. Therefore, the inhibiting phenomenon by cations may be caused by the presence of Cl^- . The Cr(VI) removal rates in Mg^{2+} and Ca^{2+} -containing systems are better than that in K^+ and Na^+ -containing systems, which may be due to the higher affinity of higher valence cations for $\text{Cr}_2\text{O}_7^{2-}$, and enhances anion transfer rate in solution. For the same valence state, the larger the ion radius ($\text{K}^+ > \text{Na}^+$ or $\text{Ca}^{2+} > \text{Mg}^{2+}$), the ion center contains more positive charge which promotes the anions' adsorption [39].

Additionally, the reusability of the Ag@TiO_2 photocatalyst was also evaluated. The performance of Ag@TiO_2 nanocomposite within five recycles is shown in Figure 6a. Obviously, the removal efficiency slowly decreases with the recycling continuing. It may be due to that the increasing amount of adsorbed Cr(III) on Ag@TiO_2 which will inhibit its surface adsorption and active site reduction properties. To further identify the adsorbed species on the catalyst surface, high resolution XPS spectra of the dry Ag@TiO_2 sample after the reaction were used to characterize the changes in the catalyst surface. The XPS spectra of Cr peaks were obviously presented in Figure 6b. The bands at binding energy of 577.2 eV and 585.9 eV were attributed to Cr(III) $2p_{3/2}$ and Cr(III) $2p_{1/2}$, respectively. The peaks at 580.6 eV belonged to the Cr(VI) $2p_{3/2}$. The results show that the adsorption and reduction were simultaneously carried out during the Cr(VI) photoreduction and the generated Cr(III) was also adsorbed on the Ag@TiO_2 surface, which results in a low Cr(VI) reduction rate. Second, it was found that the XPS of Ag shifted to a certain extent after the reaction (Figure S5), indicating that more Ag_2O was produced. It is possible that the ability to transfer electrons might decreased, which will lead to a decline in catalytic performance. However, after five consecutive cycles, Ag@TiO_2 removal rate could still reach 62%, indicating that the resultant photocatalyst has a relatively good reusability.

It is well known that the selective adsorption of Cr(VI) and the desorption of Cr(III) at the surface of photocatalysts are very important factors in determining the photocatalytic reduction. The modification of Ti^{3+} and hydroxyl groups can enhance the positive charge on the surface of the catalyst and further increase the preferential adsorption of Cr(VI) and repulsion of Cr(III) by electrostatic action [40]. Moreover, it might be a simpler way to make the catalyst aspects of active-site reusable by external force, like: thermal, chemical reactivation, calcine, and Ultrasonic cleaning et al.

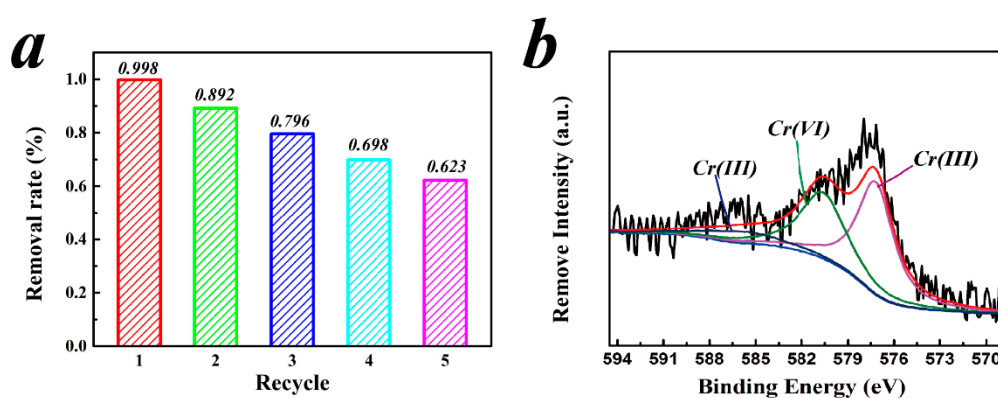


Figure 6. (a) The reusability of synthetic catalysts by 5 recycle on Cr(VI) removal (using the Ag@TiO_2 with 0.06 wt %); (b) High resolution XPS of Cr on the surface of Ag@TiO_2 catalyst. The experimental conditions were $[\text{Cr(VI)}]_0 = 10 \text{ mg/L}$.

2.3. Kinetic Modeling Study

The reaction between Ag@TiO_2 photocatalysts and Cr(VI) was related to the multiphase surface reaction. Langmuir-Hinshelwood first order kinetic model was applied to evaluate the reaction kinetics.

$$r_0 = -\frac{dC}{dt} = \frac{kKC_s}{1 + KC_s} \quad (1)$$

where r_0 is the initial photocatalytic reduction efficiency (mg/L·min); t is the reaction time (min); k is the reaction efficiency constant (min^{-1}); K is the reaction equilibrium constant; and C_s is the reactant concentration (mg/L); k and K are determined by many factors in the reaction system, including the amount of catalyst, light intensity, initial concentration of reactants, reaction temperature, physical properties of the reactants, gas phase oxygen concentration, etc.

When the reaction substrate concentration is rather low, $KC \ll 1$, the equation can be simplified to the apparent first order equation:

$$r_0 = -\frac{dC}{dt} = kKC = k_{ap}C \quad (2)$$

where k_{ap} is the apparent rate constant of a pseudo first order reaction. In the beginning of the reaction, $t = 0$, $C_t = C_0$, the equation can be obtained after deformation:

$$\ln\left(\frac{C_t}{C_0}\right) = -k_{ap}t + b \quad (3)$$

where C_t is the concentration of Cr(VI) in the solution at t min; C_0 is the initial Cr(VI) concentration; b represents a constant; k_{ap} is the apparent rate constant (min^{-1}).

From Figure 7, it can be seen that $\ln(C_t/C_0) - t$ is in a good linear relationship and its performance fits the first order reaction. The apparent reaction kinetic constant can be applied to estimate the total reaction rate, and then compare the photocatalytic efficiency under different conditions. In Figure 7, initial pH and Ag loading affected the obtained reaction kinetic constant. The first-order kinetic equation, reaction rate constant, reaction rate and the correlation coefficients (R^2) of the photocatalytic reaction under different conditions are shown in Table 2. It can be seen that the apparent rate constant k_{ap} decreases as initial pH grows, and k_{ap} under acidic condition (pH = 3) was about six times as much as the neutral one (pH = 7) and quickly dropped to about zero under alkaline conditions (pH = 11), indicating that acidic environment promotes the photocatalytic reduction processes. In addition, k_{ap} presents a trend that gradually rises to 0.0534 min^{-1} until the silver doping ratio reaches 0.06 wt % and then continuously decreases to 0.0211 min^{-1} as the Ag loading grows to 3.0 wt %. Furthermore, the results show that Cr(VI) reduction efficiency by 0.06 wt % Ag loading was 2.5 times compared to pure TiO_2 , indicating that suitable Ag loading on TiO_2 surface promoted its photocatalytic ability significantly.

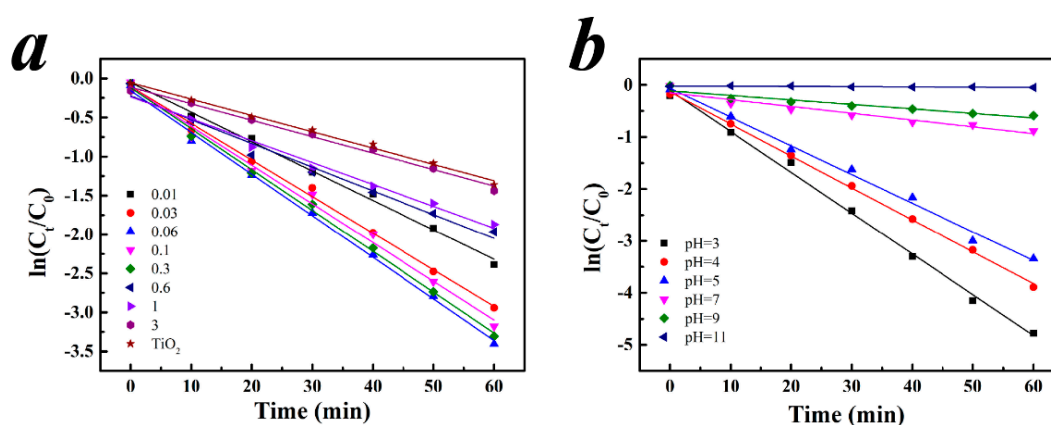


Figure 7. The study of kinetics at different Ag loadings (a) and pH values (b).

Table 2. The relevant parameters obtained from kinetic study.

	Kinetics Equation	k_{ap} (min^{-1})	r_0 ($\text{mg/L}\cdot\text{min}$)	R^2
0.01 wt %	$\ln(C_t/C_0) = 0.0377t - 0.0549$	0.0377	0.3770	0.9947
0.03 wt %	$\ln(C_t/C_0) = 0.0470t - 0.1046$	0.0470	0.4700	0.9954
0.06 wt %	$\ln(C_t/C_0) = 0.0534t - 0.1572$	0.0534	0.5340	0.9966
0.1 wt %	$\ln(C_t/C_0) = 0.0497t - 0.1149$	0.0497	0.4970	0.9895
0.3 wt %	$\ln(C_t/C_0) = 0.0525t - 0.1183$	0.0525	0.5250	0.9963
0.6 wt %	$\ln(C_t/C_0) = 0.0304t - 0.2233$	0.0304	0.3040	0.9731
1 wt %	$\ln(C_t/C_0) = 0.0281t - 0.2356$	0.0281	0.2810	0.9858
3 wt %	$\ln(C_t/C_0) = 0.0211t - 0.1137$	0.0211	0.2110	0.9909
Bare	$\ln(C_t/C_0) = 0.0209t - 0.0562$	0.0209	0.2090	0.9937
pH = 3	$\ln(C_t/C_0) = 0.0786t - 0.1070$	0.0786	0.7860	0.9954
pH = 4	$\ln(C_t/C_0) = 0.615t - 0.1347$	0.0615	0.6150	0.9989
pH = 5	$\ln(C_t/C_0) = 0.0552t - 0.0652$	0.0552	0.5520	0.9920
pH = 7	$\ln(C_t/C_0) = 0.0131t - 0.1523$	0.0131	0.1310	0.9213
pH = 9	$\ln(C_t/C_0) = 0.0086t - 0.1151$	0.0086	0.0860	0.9039
pH = 11	$\ln(C_t/C_0) = -0.0222$	0.0001	0.0010	0.5126
Na ⁺	$\ln(C_t/C_0) = 0.0189t - 0.0560$	0.0189	0.1890	0.9948
K ⁺	$\ln(C_t/C_0) = 0.0175t - 0.0836$	0.0175	0.1750	0.9881
Ca ²⁺	$\ln(C_t/C_0) = 0.0202t - 0.0607$	0.0202	0.2020	0.9915
Mg ²⁺	$\ln(C_t/C_0) = 0.0209t - 0.0890$	0.0209	0.2090	0.9895
SO ₄ ²⁻	$\ln(C_t/C_0) = 0.0234t - 0.1560$	0.0234	0.2340	0.9808
NO ₃ ⁻	$\ln(C_t/C_0) = 0.0320t - 0.1758$	0.0320	0.3202	0.9843
Cl ⁻	$\ln(C_t/C_0) = 0.0190t - 0.0600$	0.0190	0.1900	0.9948

2.4. Mechanism of Photoreduction

To identify the radical species involved in the reduction of Cr(VI) by Ag@TiO₂ system, EPR experiments using DMPO as the spin-trapping agent were carried out. EPR analysis results of TiO₂ and Ag@TiO₂ solids are shown in Figure 8a; it can be clearly seen that one signal appeared after UV irradiation both for bare TiO₂ and Ag@TiO₂; the g-factors were 2.0024 and 2.0019, respectively, which was considered to be a free electron in the conduction band of TiO₂ or an oxyanion vacancy. The enhancement of the peak signal intensity proves that more free electrons and oxygen vacancies are generated in the Ag@TiO₂ system, which may be due to the photogenerated electrons being transferred to silver elements and stored therein.

Figure 8c,d shows the EPR spectra of DMPO-trapped O₂^{•-} in methanol medium and DMPO-trapped •OH in aqueous medium which have been investigated in the active radical species for the TiO₂ and Ag@TiO₂. It be able to evidently noted that four characteristic peaks (1:2:2:1) of DMPO-•OH adducts and six characteristic peaks of the DMPO-O₂^{•-} adducts were observed on TiO₂ or Ag@TiO₂ nanocomposite systems under UV light irradiation, but no signal was detected in the dark. It could be noted that, the intensity signals of the hydroxyl radical and superoxide radical species formed in Ag@TiO₂ were stronger than those in TiO₂ under UV irradiation, which represent the sample of Ag@TiO₂ effectively promoted electron/hole pair separation and prolonged the lifetime. This, in turn, explains why there is a higher photocatalytic activity of Ag@TiO₂ than TiO₂ toward the contaminants removal.

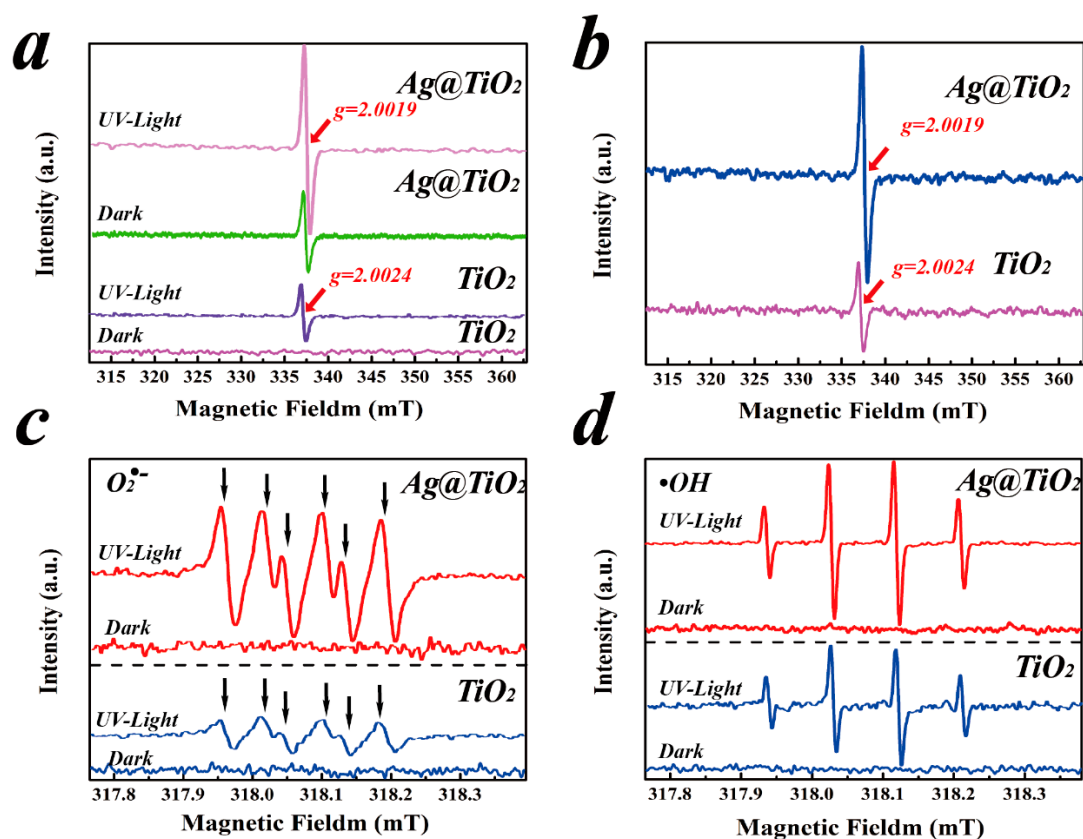


Figure 8. (a) EPR spectra in activation of the as prepared Ag@TiO₂ (0.06 wt %) and pure TiO₂ powder; (b) EPR difference spectrum between dark and UV-light of TiO₂ and Ag@TiO₂; (c) EPR spectra of radical adducts trapped by DMPO in TiO₂ and Ag@TiO₂ dispersions under UV light irradiation: DMPO-O₂^{•-} formed in irradiated methanol dispersions; (d) DMPO-•OH formed in irradiated aqueous dispersions. Reaction conditions: [Ag@TiO₂] = 1 mg/mL, [TiO₂] = 1 mg/mL, [DMPO] = 100 mM, [Illumination time] = 5 min.

To further identify the elemental constitution and its valences, the resultant Ag@TiO₂ photocatalyst was characterized via XPS spectra. The full spectrum of TiO₂ loaded with Ag nanoparticles was illustrated in Figure 9a and Figure S6, the main elements were Ti, O, C and Ag. The C emergence is due to the introduction of exogenous substances during the testing processes. As presented in Figure 9b, it can be seen that the loading of silver nanoparticles has obvious effects on the binding of Ti 2*p* orbitals. Compared with pure TiO₂, the combination of Ti 2*p*_{1/2} and Ti 2*p*_{3/2} can change from to 465.13 eV and 459.45 eV to 458.77 eV and 464.57 eV, respectively. The affection was due to that the load of Ag makes the heterojunction between Ag and TiO₂, and the plasmonic effect produced by Ag makes the electron field which would influence TiO₂. Figure 9c shows the XPS peak of O 1s, from which we can find the asymmetry peak of O. Therefore, two peaks were obtained by Gauss Lorentz method. The peaks at 531.87 eV and 530.79 eV were assigned to Ti-OH bond and the Ti-O-Ti bond in lattice oxygen, respectively. The binding energy at 533.57 eV was due to the adsorbed oxygen on the catalyst surface. The X-ray spectrum of Ag 3*d* is shown in Figure 9d, indicating that the XPS peak of Ag 3*d* mainly contains two characteristic peaks. The binding energies of Ag 3*d*_{3/2} and Ag 3*d*_{5/2} were observed at 368.2 eV and 374.2 eV, respectively. The results showed that the difference of binding energies between Ag 3*d*_{5/2} and Ag 3*d*_{3/2} was 6.1 eV, revealing that the Ag element depositing on TiO₂ surface exists in the form of zero valences, which was reported in the previous literature [27,41]. To further elucidate the surface metal composition, Ag 3*d* peaks of the catalysts were deconvoluted,

and the content of Ag was calculated to be 0.6655% (Table S3). Combined with the XRD and HRTEM results, the existence of Ag and TiO₂ nanoparticles in the resultant compound can be further proved.

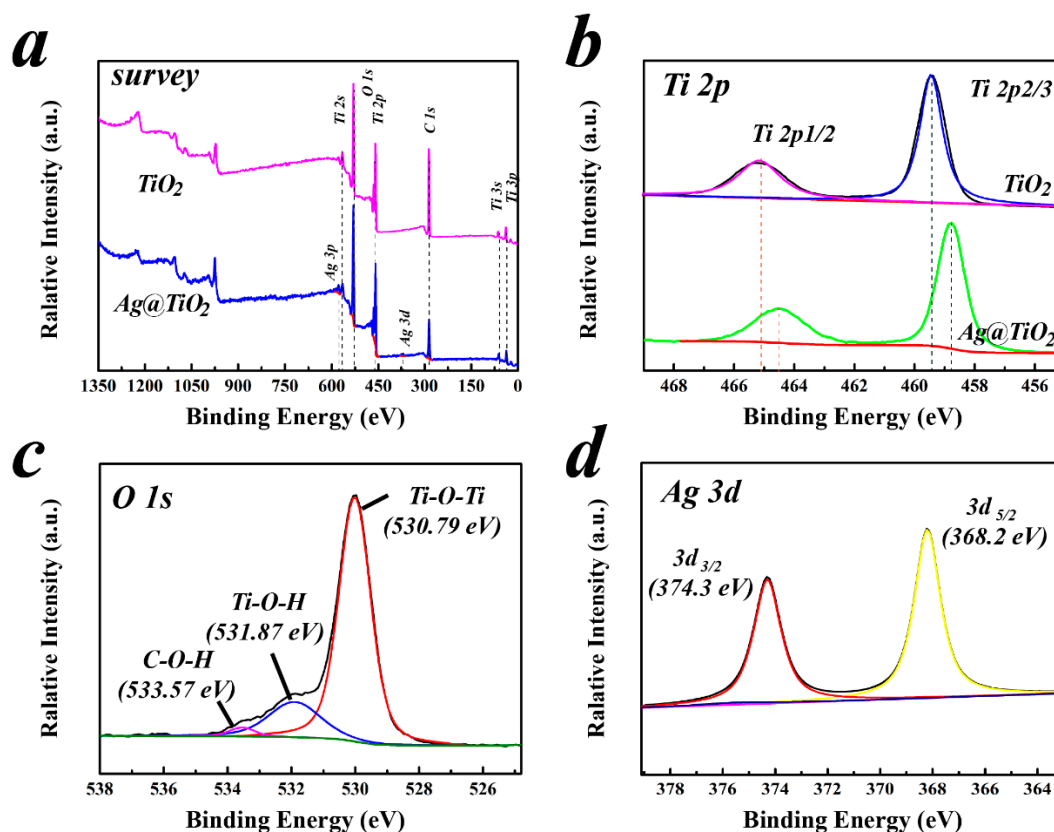


Figure 9. The survey spectrum (a); Ti 2p (b), O 1s (c), and Ag 3d (d) XPS spectra of the Ag@TiO₂ composites (0.6 wt %, 30 min irradiation).

The photocatalytic reaction was considered to be a heterogeneous interfacial reaction, and mainly contained two parts of the reaction mechanism (Figure 10). Firstly, the good adsorption of Cr(VI) on the surface of Ag@TiO₂ was a prerequisite of photoreduction. Then, the Cr(VI) was reduced to Cr(III) by using photogenerated electrons from the light source. Adsorption of oxygen on the catalyst surface as an electron competitor was generally considered to have the potential to reduce the rate in the photoreduction reaction. Oxygen reduction state (O₂^{•−}) can promote the photoreduction of Cr(VI) in TiO₂ system as electron transfer intermediates [42]. From the results of photoreduction experiments and the EPR spectra of DMPO-trapped O₂^{•−}, it can be seen that a substantial increase of O₂^{•−} did not inhibit the reduction activity of photocatalysis, which may indicate the O₂^{•−} as a reduced product formed by obtaining electrons and also has strong reducibility, resulting in the transformation of Cr(VI), a strongly oxidizing species, to Cr(III). Therefore, the photoreduction of Cr(VI) by Ag@TiO₂ system under UV light is a complex synergistic processes with multi-actions. However, more photogenerated electrons were probably exposed, and resulted in a higher photocatalytic activity due to the loading of Ag on TiO₂.

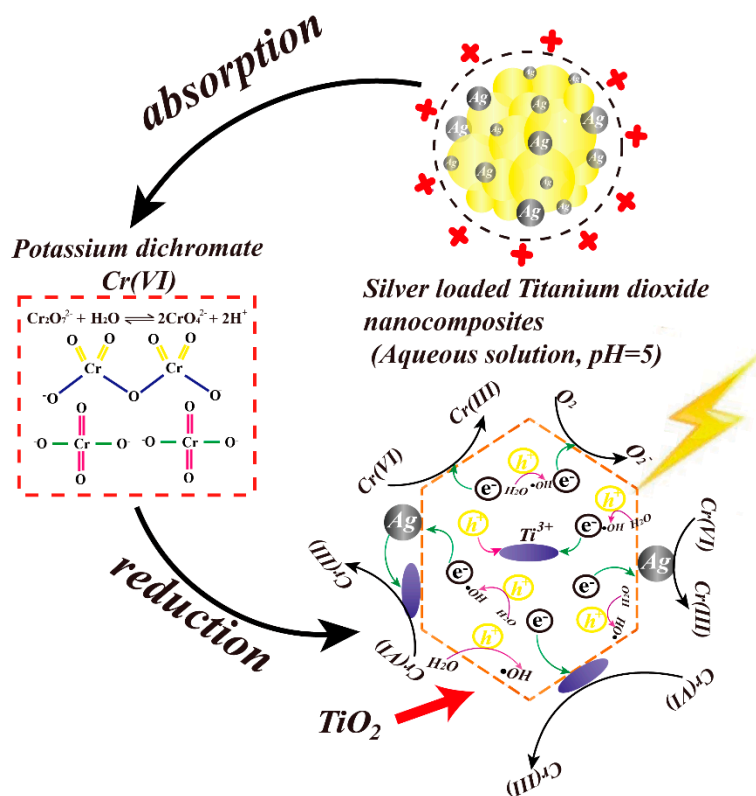


Figure 10. Mechanism of Cr(VI) photoreduction by ultra-trace Ag enhanced TiO₂ composites. 3. Materials and Methods.

3. Materials and Methods

3.1. Materials

Potassium dichromate (K₂Cr₂O₇), sodium hydroxide (NaOH), hydrochloric acid (HCl, 36.0–38.0%) were all of analytical grade. Absolute ethanol (C₂H₅OH) was premium grade pure. All of the chemicals above were purchased from Kelong Chemical Reagent Company (Sichuan, China). TiO₂ (P25) nanoparticles powder was supplied by Degussa Company (Essen, Germany), which is a mixture of anatase and rutile (8:2) with primary particle sizes of 20–30 nm. Silver nitrate (AgNO₃) was obtained from Aladdin Industrial Corporation (Shanghai, China). Deionized (D.I.) water was produced by Ulupure Milli-Q water purification system.

3.2. Preparation of Ag@TiO₂ Photocatalyst via Ultrasonic Impregnation Assisted Photoreduction Deposition

Silver was deposited onto the surface of TiO₂ formed via a “green” ultrasonic impregnation assisted photoreduction strategy. Firstly, a suspension of titanium dioxide nanoparticles (P25, 10 g/L) with absolute ethanol solution (different concentrations of ethanol solution ca. 0%, 25%, 50%, 75% and 100%, as an electron donor) and a precious metal precursor solution (AgNO₃ 0.074 mM) were stirred and ultrasound 30 min under dark conditions. Then, the suspension was transferred to a quartz reactor under UV irradiation (300 W mercury lamp) for another 30 min. Finally, the obtained Ag@TiO₂ nanocomposites were filtered and washed with a large amount of ultrapure water to remove unreacted silver nitrate, and freeze-dried for further experiments. A typical silver loading was evaluated to be ca. 0.0648 wt % (Ag/TiO₂) by using ICP-AES (Table 1).

3.3. Batch Experiments of Photoreduction

The prepared photocatalyst was suspended in a quartz reactor containing 50 mL (10 mg/L) target contamination (Cr(VI)). The suspension was dispersed for about 2 min by ultra-sonication before irradiation, and then stirred in the dark for 30 min to allow equilibrium adsorption of the heavy metal. A 300 W mercury lamp was used as a light source (irradiation about 60 min) to excite TiO₂ to generate photo-generated electrons and photogenerated holes to reduce heavy metals. Effects of silver load, pH, catalyst dosage and coexisting ions on Cr(VI) reduction were fully considered. A 20 mg/L Cr(VI) aqueous solution was diluted from 100 mg/L Cr(VI) stock solution in 1 L ultra-pure water before experiments. The pH was monitored by PHS-320 and adjusted by 1.0 M HCl or NaOH. The sample aliquots were intermittently (0, 10, 20, 30, 40, 50 and 60 min) withdrawn and filtered through a 0.45- μ m aqueous syringe filter for the analysis of Cr(VI) using the DPC (diphenyl-carbazide) method at 540 nm (UV-vis spectrophotometer).

3.4. Catalyst Characterization and Involved Analytical Method

The crystal structure of Ag@TiO₂ was characterized by Ultima IV XRD (Rigaku Corp., Tokyo, Japan) employing Cu K α radiation ($\lambda = 0.154$ nm, 40 KV) in the range of 3° to 80°. The micromorphology was observed by JEM2100 TEM (JEOL, Tokyo, Japan) operated at 200 kV. XPS measurements were performed by a K-Alpha Probe (Thermo Scientific, Waltham, MA, USA) with a monochromated Al-K α radiation (300 W). UV-vis spectra was obtained on a spectrophotometer (Shanghai United Instrument Corp., Ltd., Shanghai, China). Zeta Potential (ZP) of the nanoparticles was determined by Malvern Zeta Sizer Nano series 3600 (Malvern Instruments Ltd., Worcestershire, UK). The BET surface area was measured at 77 K using F-Sorb 2400 N₂ adsorption analysis (Gold APP Instruments, Beijing, China).

Electron paramagnetic resonance spectra (EPR) was performed on an EMX-8 spectrometer (Bruker BioSpin Corp., Karlsruhe, Germany). First, the sample was dispersed in aqueous solution (1 mg/mL) and dispersed by ultrasonic uniformity; Second, add DMPO (100 mM) and mix well; Third, the mixed sample was placed in a flat pool, and then set in the instrument test chamber; Fourth, in situ lighting test (5 min) and record the data.

Inductively coupled plasma atomic emission spectrometry (ICP-AES) was used to evaluate the Ag amount in the obtained photocatalyst by Agilent 720 (Agilent Technologies Inc., Palo Alto, CA, USA). First, 0.0164 g Ag@TiO₂ was dissolved in aqua regia and boiled. After cooling, set it in a 50 mL volumetric flask. Then, dilutes the solution according to different dilution factors for detection. At last, record the data on the display. The conversion is obtained from the readings and the actual participating of samples.

4. Conclusions

Based on ultrasonic impregnation-assisted UV-photoreduction, Ag⁺ could be fully reduced via a facile in-situ synthetic approach toward ultra-trace silver-doped TiO₂ photocatalysts without using any reducing agents. The results demonstrated that all obtained Ag@TiO₂ photocatalysts have a significant photocatalytic activity compared to commercial P25 nanoparticles in the reduction of Cr(VI), which is interpreted as the loading of Ag being used as an intermediary container for electron transfer and storage to promote the separation of photogenerated e^- and h^+ . The Langmuir-Hinshelwood kinetic model can well explain the removal kinetics of Cr(VI) reduction. Regeneration performance of Ag@TiO₂ indicated that the photocatalyst still maintained a rather high catalytic activity after five cycles (62%) and could be reused. Taking the practical application of photocatalytic removal of wastewater into account, the solution pH, coexistence of ions, dosing and other factors were considered, which will provide a useful guide for further reaction model simulation. The facile-fast, low-cost and eco-friendly method of synthesizing Ag@TiO₂ nanomaterials can provide a valid strategy for

the broad-scale preparation of precious metal matrix composites, and might be used as a promising photocatalyst for wastewater treatment.

Supplementary Materials: The following are available online at <http://www.mdpi.com/2073-4344/8/6/251/s1>. **Table S1** BET data for different silver loadings. **Table S2** BET data for different solvent concentration. **Table S3** XPS date of atomic (Ag@TiO₂, 0.6 wt %). **Figure S1** The Energy Dispersive Spectrometer of Ag@TiO₂ catalyst. **Figure S2** XRD patterns of the Ag@TiO₂ nanocomposites, in which A is anatase phase and R is rutile phase. **Figure S3** Effect of different concentration of empty scavenger (Ethanol) on Cr reduction. **Figure S4** Zeta potential of bare TiO₂ and Ag@TiO₂ catalyst. **Figure S5** High resolution XPS of Ag 3d of Ag@TiO₂ catalyst before (a) and after (b) reaction. **Figure S6** The survey spectrum XPS spectra of the Ag@TiO₂ composites.

Author Contributions: S.P., R.Z., and W.C. initiated the concept; S.P. and Y.H. designed and conceived of the experiments; Y.H. and H.C. performed the experiments; S.P., Y.H. and Z.Y. analyzed the data; H.C., R.Z., and D.D. performed the characterizations, interpreted the data; S.P. contributed reagents/materials/analysis tools; S.P., Y.H. and S.X. drafted the manuscript, W.C. and Z.D. corrected the manuscript. All authors read and approved the final manuscript.

Funding: This research received no external funding.

Acknowledgments: The authors thank Anatoly ZINCHENKO for a helpful discussion. This work was supported by the National Natural Science Foundation of China (No. 41772264) and the Research Fund of State Key Laboratory of Geohazard Prevention and Geoenvironment Protection (SKLGP2018Z006). Wei Chu.

Conflicts of Interest: The authors declare no conflict of interest.

References

1. De Flora, S.; Bagnasco, M.; Serra, D.; Zancchi, P. Genotoxicity of chromium compounds. A review. *Mutat. Res.* **1990**, *238*, 99–172. [[CrossRef](#)]
2. Ellis, A.S.; Bullen, T.D. Chromium isotopes and the fate of hexavalent chromium in the environment. *Science* **2002**, *295*, 2060–2062. [[CrossRef](#)] [[PubMed](#)]
3. Kebir, M.; Chabani, M.; Nasrallah, N.; Bensmaili, A.; Trari, M. Coupling adsorption with photocatalysis process for the Cr(VI) removal. *Desalination* **2011**, *270*, 166–173. [[CrossRef](#)]
4. Cimino, G.; Passerini, A.; Toscano, G. Removal of toxic cations and Cr(VI) from aqueous solution by hazelnut shell. *Water Res.* **2000**, *34*, 2955–2962. [[CrossRef](#)]
5. Sheng, G.; Hu, J.; Li, H.; Li, J.; Huang, Y. Enhanced sequestration of Cr(VI) by nanoscale zero-valent iron supported on layered double hydroxide by batch and XAFS study. *Chemosphere* **2016**, *148*, 227–232. [[CrossRef](#)] [[PubMed](#)]
6. Yang, L.; Zheng, X.; Liu, M.; Luo, S.; Luo, Y.; Li, G. Fast photoelectro-reduction of Cr(VI) over MoS₂@TiO₂ nanotubes on Ti wire. *J. Hazard. Mater.* **2017**, *329*, 230–240. [[CrossRef](#)] [[PubMed](#)]
7. Bhowal, A.; Datta, S. Studies on transport mechanism of Cr(VI) extraction from an acidic solution using liquid surfactant membranes. *J. Membr. Sci.* **2001**, *188*, 1–8. [[CrossRef](#)]
8. Chuang, S.M.; Vinh, Y.; Feng, C.L.; Lee, S.J.; Choo, K.H.; Li, C.W. Electrochemical Cr(VI) reduction using a sacrificial Fe anode: Impacts of solution chemistry and stoichiometry. *Sep. Purif. Technol.* **2017**, *191*, 167–172. [[CrossRef](#)]
9. Alowitz, M.J.; Scherer, M.M. Kinetics of nitrate, nitrite, and Cr(VI) reduction by iron metal. *Environ. Sci. Technol.* **2002**, *36*, 299–306. [[CrossRef](#)] [[PubMed](#)]
10. Pu, S.; Xiang, C.; Zhu, R.; Ma, H.; Zinchenko, A.; Chu, W. An efficient heterogeneous Fenton catalyst based on modified diatomite for degradation of cationic dye simulated wastewater. *Desalin. Water Treat.* **2017**, *79*, 378–385. [[CrossRef](#)]
11. Gheju, M.; Balcu, I. Removal of chromium from Cr(VI) polluted wastewaters by reduction with scrap iron and subsequent precipitation of resulted cations. *J. Hazard. Mater.* **2011**, *196*, 131–138. [[CrossRef](#)] [[PubMed](#)]
12. Ma, H.; Pu, S.Y.; Ma, J.; Yan, C.; Zinchenko, A.; Pei, X.J.; Chu, W. Formation of multi-layered chitosan honeycomb spheres via breath-figure-like approach in combination with co-precipitation processing. *Mater. Lett.* **2018**, *211*, 91–95. [[CrossRef](#)]
13. Hu, J.; Chen, G.; Lo, I.M. Removal and recovery of Cr(VI) from wastewater by maghemite nanoparticles. *Water Res.* **2005**, *39*, 4528–4536. [[CrossRef](#)] [[PubMed](#)]
14. Galán, B.; Castañeda, D.; Ortiz, I. Removal and recovery of Cr(VI) from polluted ground waters: A comparative study of ion-exchange technologies. *Water Res.* **2005**, *39*, 4317–4324. [[CrossRef](#)] [[PubMed](#)]

15. Barrera, C. A review of chemical, electrochemical and biological methods for aqueous Cr(VI) reduction. *J. Hazard. Mater.* **2012**, *1*, 223–224.
16. Chen, D.; Ray, A.K. Removal of toxic metal ions from wastewater by semiconductor photocatalysis. *Chem. Eng. Sci.* **2001**, *56*, 1561–1570. [[CrossRef](#)]
17. Minero, C.; Mariella, G.; Maurino, V.; Vione, A.D.; Pelizzetti, E. Photocatalytic Transformation of Organic Compounds in the Presence of Inorganic Ions. 2. Competitive Reactions of Phenol and Alcohols on a Titanium Dioxide-Fluoride System. *Langmuir* **2015**, *16*, 8964–8972. [[CrossRef](#)]
18. Zhang, Y.; Chen, Z.; Liu, S.; Xu, Y.J. Size effect induced activity enhancement and anti-photocorrosion of reduced graphene oxide/ZnO composites for degradation of organic dyes and reduction of Cr(VI) in water. *Appl. Catal. B* **2013**, *140–141*, 598–607. [[CrossRef](#)]
19. Mirghani, M.; Al-Mubaiyedh, U.A.; Nasser, M.S.; Shawabkeh, R. Experimental study and modeling of photocatalytic reduction of Pb²⁺ by WO₃/TiO₂ nanoparticles. *Sep. Purif. Technol.* **2015**, *14*, 285–293. [[CrossRef](#)]
20. Sreekantan, S.; Lai, C.W.; Zaki, S.M. The Influence of Lead Concentration on Photocatalytic Reduction of Pb(II) Ions Assisted by Cu-TiO₂ Nanotubes. *Int. J. Photoenergy* **2014**, *2014*, 839106. [[CrossRef](#)]
21. Dozzi, M.V.; Marzorati, S.; Longhi, M.; Coduri, M.; Artiglia, L.; Selli, E. Photocatalytic activity of TiO₂-WO₃ mixed oxides in relation to electron transfer efficiency. *Appl. Catal. B* **2016**, *186*, 157–165. [[CrossRef](#)]
22. Dozzi, M.V.; Saccomanni, A.; Selli, E. Cr(VI) photocatalytic reduction: Effects of simultaneous organics oxidation and of gold nanoparticles photodeposition on TiO₂. *J. Hazard. Mater.* **2012**, *99*, 188–195. [[CrossRef](#)] [[PubMed](#)]
23. Matamoros-Ambrocio, M.; Ruiz-Peralta, M.; Chigo-Anota, E.; García-Serrano, J.; Pérez-Centeno, A.; Sánchez-Cantú, M.; Rubio-Rosas, E.; Escobedo-Morales, A. A Comparative Study of Gold Impregnation Methods for Obtaining Metal/Semiconductor Nanophotocatalysts: Direct Turkevich, Inverse Turkevich, and Progressive Heating Methods. *Catalysts* **2018**, *8*, 161. [[CrossRef](#)]
24. Ku, Y.; Jung, I.L. Photocatalytic reduction of Cr(VI) in aqueous solutions by UV irradiation with the presence of titanium dioxide. *Water Res.* **2001**, *35*, 135–142. [[CrossRef](#)]
25. Colón, G.; Hidalgo, M.C.; Navió, J.A. Photocatalytic deactivation of commercial TiO₂ samples during simultaneous photoreduction of Cr(VI) and photooxidation of salicylic acid. *J. Photochem. Photobiol.* **2001**, *138*, 79–85. [[CrossRef](#)]
26. Zheng, Z.; Huang, B.; Qin, X.; Zhang, X.; Dai, Y.; Whangbo, M.H. Facile in situ synthesis of visible-light plasmonic photocatalysts M@TiO₂ (M = Au, Pt, Ag) and evaluation of their photocatalytic oxidation of benzene to phenol. *J. Mater. Chem.* **2011**, *21*, 9079–9087. [[CrossRef](#)]
27. Cheng, B.; Le, Y.; Yu, J. Preparation and enhanced photocatalytic activity of Ag@TiO₂ core-shell nanocomposite nanowires. *J. Hazard. Mater.* **2010**, *177*, 971–977. [[CrossRef](#)] [[PubMed](#)]
28. Hirakawa, T.; Kamat, P.V. Photoinduced electron storage and surface plasmon modulation in Ag@TiO₂ clusters. *Langmuir* **2004**, *20*, 5645–5647. [[CrossRef](#)] [[PubMed](#)]
29. Xiang, Q.; Yu, J.; Cheng, P.; Ong, H.C. Microwave-Hydrothermal Preparation and Visible-Light Photoactivity of Plasmonic Photocatalyst Ag-TiO₂ Nanocomposite Hollow Spheres. *Chem. Asian J.* **2010**, *5*, 1466–1474. [[CrossRef](#)] [[PubMed](#)]
30. Zhang, H.; Chen, G. Potent antibacterial activities of Ag/TiO₂ nanocomposite powders synthesized by a one-pot sol-gel method. *Environ. Sci. Technol.* **2009**, *43*, 2905–2910. [[CrossRef](#)] [[PubMed](#)]
31. Wang, Y.; Chao, Y.; Lei, C.; Zhang, Y.; Yang, J. Controllable Charge Transfer in Ag-TiO₂ Composite Structure for SERS Application. *Nanomaterials* **2017**, *7*, 159. [[CrossRef](#)] [[PubMed](#)]
32. Guin, D.; Manorama, S.V.; Latha, J.N.L.; Singh, S. Photoreduction of Silver on Bare and Colloidal TiO₂ Nanoparticles/Nanotubes: Synthesis, Characterization, and Tested for Antibacterial Outcome. *J. Phys. Chem. C* **2007**, *111*, 13393–13397. [[CrossRef](#)]
33. Behnajady, M.A.; Modirshahla, N.; Shokri, M.; Rad, B. Enhancement of photocatalytic activity of TiO₂ nanoparticles by Silver doping: Photodeposition versus liquid impregnation methods. *Glob. NEST J.* **2007**, *10*, 1–7.
34. Liu, L.; Liu, Z.; Bai, H.; Sun, D.D. Concurrent filtration and solar photocatalytic disinfection/degradation using high-performance Ag/TiO₂ nanofiber membrane. *Water Res.* **2012**, *46*, 1101–1112. [[CrossRef](#)] [[PubMed](#)]

35. Pu, S.Y.; Hui, M.; Zinchenko, A.; Wei, C. Novel highly porous magnetic hydrogel beads composed of chitosan and sodium citrate: An effective adsorbent for the removal of heavy metals from aqueous solutions. *Environ. Sci. Pollut. Res.* **2017**, *24*, 1–11. [[CrossRef](#)] [[PubMed](#)]
36. Deng, Z.; Ning, J.; Su, Z.; Xu, S.; Xing, Z.; Wang, R.; Lu, S.; Dong, J.; Zhang, B.; Yang, H. Structural Dependences of Localization and Recombination of Photogenerated Carriers in the top GaInP Subcells of GaInP/GaAs Double-Junction Tandem Solar Cells. *ACS Appl. Mater. Interfaces* **2015**, *7*, 690–695. [[CrossRef](#)] [[PubMed](#)]
37. Yang, C.K.; Wang, S.F.; Tsai, H.Y.; Lin, S.Y. Intrinsic photocatalytic oxidation of the dye adsorbed on TiO₂ photocatalysts by diffuse reflectance infrared Fourier transform spectroscopy. *Appl. Catal. B* **2001**, *30*, 293–301. [[CrossRef](#)]
38. Davis, R.J.; Gainer, J.L.; O’Neal, G.; Wu, I.W. Photocatalytic Decolorization of Wastewater Dyes. *Water Environ. Res.* **1994**, *66*, 50–53. [[CrossRef](#)]
39. Pu, S.; Wang, M.; Wang, K.; Hou, Y.; Yu, J.; Shi, Q.; Pei, X.; Chu, W. Preparation of CS-Fe@Fe₃O₄ nanocomposite as an efficient and recyclable adsorbent for azo dyes removal. *Desalin. Water Treat.* **2018**, *95*, 319–332. [[CrossRef](#)]
40. Li, Y.; Bian, Y.; Qin, H.; Zhang, Y.; Bian, Z. Photocatalytic reduction behavior of hexavalent chromium on hydroxyl modified titanium dioxide. *Appl. Catal. B* **2017**, *206*, 293–299. [[CrossRef](#)]
41. Lei, X.F.; Xue, X.X.; Yang, H. Preparation and characterization of Ag-doped TiO₂ nanomaterials and their photocatalytic reduction of Cr(VI) under visible light. *Appl. Surf. Sci.* **2014**, *321*, 396–403. [[CrossRef](#)]
42. Aguado, M.A.; GimãNez, J.; Cervera-March, S. Continuous photocatalytic treatment of Cr(VI) effluents with semiconductor powders. *Chem. Eng. Commun.* **1991**, *104*, 71–85. [[CrossRef](#)]



© 2018 by the authors. Licensee MDPI, Basel, Switzerland. This article is an open access article distributed under the terms and conditions of the Creative Commons Attribution (CC BY) license (<http://creativecommons.org/licenses/by/4.0/>).